Corner-Cube Retroreflectors Based on Structure-Assisted Assembly for Free-Space Optical Communication

Lixia Zhou, Joseph M. Kahn, *Fellow, IEEE*, and Kristofer S. J. Pister, *Member, IEEE*

***Abstract*—We have fabricated sub-millimeter-sized quad corner-cube retroreflectors (CCRs) for free-space optical communication. Each quad CCR structure comprises three mirrors micromachined from silicon-on-insulator wafers, and is designed to facilitate manual assembly with accurate angular alignment. Assembled CCRs exhibit mirror nonflatness less than 50 nm, mirror roughness less than 2 nm, and mirror misalignment less than 1 mrad, leading to near-ideal optical performance. The quad CCR incorporates a gap-closing actuator to deflect a base mirror common to the four CCRs, allowing their reflectivity to be modulated up to 7 kb/s by a drive voltage less than 5 V. We have demonstrated a 180-m free-space optical communication link using a CCR as a passive optical transmitter. Quad CCRs have been integrated into miniature, autonomous nodes that constitute a distributed wireless sensor network. We present an analysis of the signal-to-noise ratio of CCR-based links, considering the impact of CCR dimensions, ambient light noise, and other factors. [907]**

***Index Terms*—Assembly, corner-cube retroreflector, free-space communication, microelectromechanical systems (MEMS).**

I. Introduction

FREE-SPACE optical communication has attracted considerable attention for a variety of applications, such as metropolitan network extensions, last-mile Internet access, and inter-satellite communication [1]–[3]. In most free-space systems, the transmitter light source is intensity modulated to encode digital signals. Zwirn proposed to use a microfabricated corner-cube retroreflector (CCR) as a free-space optical transmitter [4]. An ideal CCR consists of three mutually orthogonal mirrors that form a concave corner. Light incident on an ideal CCR (within an appropriate range of angles) is reflected back to the source. By misaligning one of the three mirrors, an on-off-keyed digital signal can be transmitted back to the interrogating light source. Such a CCR has been termed a "passive optical transmitter" because it can transmit without incorporating a light source. An electrostatically actuated CCR transmitter offers the advantages of small size, excellent optical performance, low power consumption and convenient integration with solar cells, sensors and CMOS control circuits. CCR transmitters have been employed in miniature, autonomous sensor nodes ("dust motes") in the Smart Dust project [5].

Fabrication of three-dimensional structures with precisely positioned out-of-plane elements poses challenges to current microelectromechanical system (MEMS) technologies. One way to achieve three-dimensional structures is to rotate parts out-of-plane on hinges [6]. However, hinges released from surface-micromachined processes typically have gaps, permitting motion between linked parts. Previous CCRs have been fabricated in the MUMPS process [7] and side mirrors were rotated out-of-plane on hinges. These CCRs had nonflat mirror surfaces and high actuation voltages. Most importantly, the hinges were not able to provide sufficiently accurate mirror alignment. In this paper, we introduce a new scheme, structure-assisted assembly, to fabricate and assemble CCRs that achieve accurate alignment of out-of-plane parts. The optical and electrical properties of CCRs produced through this method are far superior to previous CCRs fabricated in the MUMPS process. Improvements include a tenfold reduction in mirror curvature, a threefold reduction in mirror misalignment, a fourfold reduction in drive voltage, an eightfold increase in resonant frequency, and improved scalability due to the quadruplet design.

We previously reported the new scheme of fabricating quad CCRs in a silicon-on-insulator (SOI) process, making use of structure-assisted assembly to achieve good mirror alignment [8]. Here we present more detailed information about the design, fabrication and performance of these quad CCRs. We describe an experimental free-space optical link using a CCR transmitter, and present an analysis of the signal-to-noise ratio (SNR) of CCR-based optical links. Fabricated CCR is incorporated with other parts of Smart Dust mote and transmits signals collected by the accelerometer and light-level sensor.

II. Design and Fabrication of CCRs

The SEM picture in Fig. 1 shows a fabricated and assembled CCR. The two side mirrors are assembled into the V-grooves on the chip, while the bottom mirror is designed to be torsionally actuated so that it can modulate the reflected light beam.

A. Design of Gap-Closing Actuator

We have chosen to fabricate CCRs in silicon-on-insulator (SOI) wafers to obtain flat and smooth mirror surfaces. The actuated mirror is fabricated in the device layer of the SOI wafer

Manuscript received July 26, 2002; revised December 5, 2002. This work was supported under the DARPA MTO MEMS Program under Contract Number DABT63-98-1-0018. Subject Editor D. Cho.

L. Zhou and K. S. J. Pister are with the Department of Electrical Engineering and Computer Sciences, University of California, Berkeley, CA 94720-1770 USA (e-mail: lzhou@eecs.Berkeley.edu; pister@eecs.Berkeley.edu).

J. M. Kahn was with the Department of Electrical Engineering and Computer Sciences, University of California, Berkeley, CA 94720-1770 USA. He is now with the Department of Electrical Engineering, Stanford University, Stanford, CA 94305-9515 USA (e-mail: jmk@ee.stanford.edu).

Digital Object Identifier 10.1109/JMEMS.2003.809956

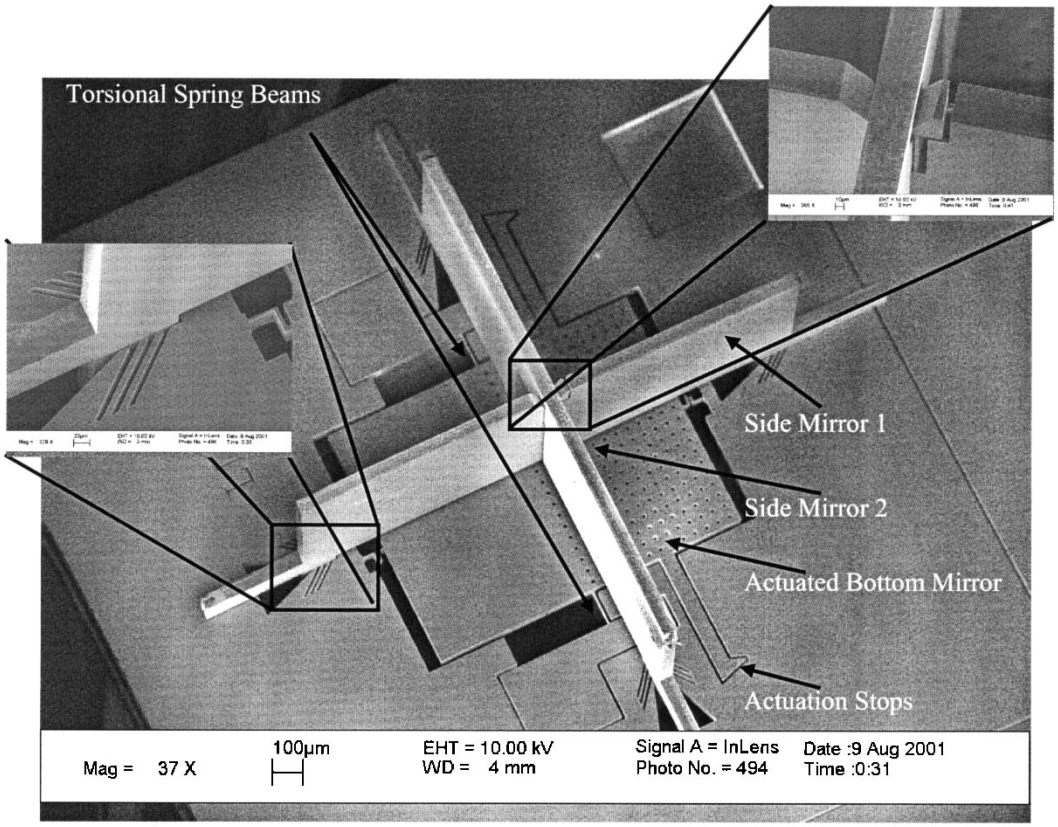

Fig. 1. SEM picture of assembled CCR quadruplet. Note the spring-locks beside the V-grooves to grab the feet of the side mirrors and the notch-protrusion clutch at the top of the side mirrors to achieve more accurate positioning. The extended beams with triangular heads act as limit stops for the gap-closing actuator, and land on electrically isolated substrate islands.

and suspended by two torsional springs. The device layer and substrate layer of the SOI wafer conveniently form the opposing electrodes of a gap-closing actuator. With half of the substrate layer under the mirror etched away, the gap-closing actuator provides a pure torsional moment. The narrow gap between the device layer and substrate layer provides an angular deflection of several mrad for a mirror plate with a side length of several hundred μm. At the same time, the narrow gap size enables high actuation moment with low drive voltage, as electrostatic actuation force inversely depends on gap size between electrodes. A second advantage of this gap-closing actuation design is that it decouples the sizing of the actuated mirror from the sizing of the actuator. With the substrate electrodes spanning from the center of the mirror plate to the root of two extended beams, the extended device layer beams act as mechanical stops to prevent shorting between the two actuator plates after pull-in. When the moving mirror reaches pull-in position, the triangular-shaped stops make point contact with electrically isolated islands on the substrate, minimizing stiction and insuring release of the mirror when the actuation voltage is removed. The amount of angular deflection and pull-in voltage depends on the position of the extended beams while the mirror plate may be larger to reflect sufficient light for the intended communication range.

B. Design of Structure-Assisted Assembly

Two groups of V-grooves are patterned in the device layer to assist in the insertion of the two side mirrors. The V-grooves are situated orthogonally around the actuated bottom mirror. Each of the side mirrors has "feet" that can be inserted manually into the larger open end of the V-grooves. The substrate under the V-grooves has been etched away to facilitate this insertion. After insertion, the side mirrors are pushed toward the smaller end of the V-grooves, where the feet are anchored by springs located next to the V-grooves. One side mirror has a notch at the top and the other side mirror has a spring-loaded protrusion at the top; after assembly, the protrusion locks into the notch, maintaining accurate alignment between the two mirrors. In this way, we can naturally fabricate four CCRs that share a common actuated bottom mirror, although the performance of those four CCRs may differ because of asymmetrical positioning of the side mirrors and the presence of etching holes on part of the actuated mirror plate. The quadruplet design increases the possibility of reflecting the light back to the base station without significantly increasing die area or actuation energy as compared to a single CCR.

C. Fabrication

The process flow is shown in Fig. 2. The fabrication starts with a double-side-polished SOI wafer with a 50 μm device layer and a 2 μm buried oxide layer. First, a layer of thermal oxide with 1 μm thickness is grown on both sides of wafer at 1100 °C. We pattern the front-side oxide with the device-layer mask. The main structure is on this layer, including the bottom mirror, two torsional spring beams suspending the

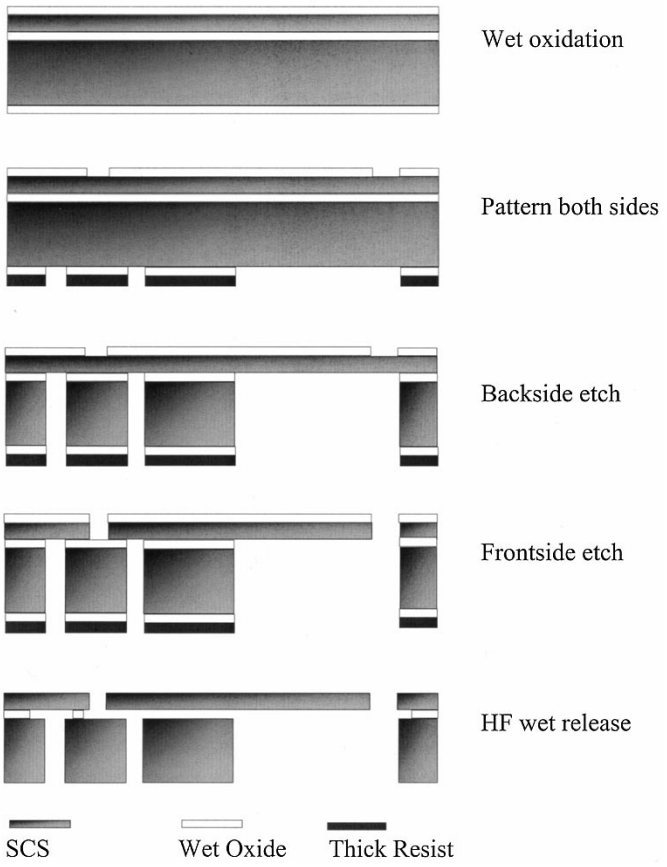

Fig. 2. Bottom mirror fabrication process. The back-side etching allows creation of electrically isolated islands in the substrate, which serve as limit stops for the gap-closing actuator when it is pulled-in. The side mirrors can be fabricated in the same process, or in a simpler single-mask process. A separate process provides more flexibility over choice of design parameters.

bottom mirror, gap-closing actuation stops and V-grooves for anchoring the side mirrors. Then we flip the wafer over, deposit thick resist and pattern the back-side oxide using the substrate-layer mask. The substrate layer functions as the second electrode of the gap-closing actuator and provides two electrically isolated islands as the pull-in stop for the actuator. We perform STS etching from the back-side first. After etching through the substrate, we continue the etching to remove the exposed buried oxide, reducing the residual stress between the buried oxide and device layer that might otherwise destroy the structures after the front-side etching. Then we etch the front-side trenches. After etching, the whole chip is dipped into concentrated HF for about 10 min, to remove the sacrificial oxide film between the bottom mirror and substrate. There is no need to employ critical-point drying after release, because the tethers between the moving mirror and the rest of the chip hold the actuated mirror in place, preventing it from being attracted to the substrate.

The side mirrors can be fabricated in the same process or by another standard single-mask process on a SOI wafer. We patterned the device layer with the shape of side mirrors, followed by a long-duration HF release. When both the bottom mirror and side mirrors are ready, we mount the side mirrors onto the bottom mirror manually to form a fully functional CCR. Fig. 3 shows the sequence of assembly. First, we pick up side mirror 1, using a pair of fine-tip tweezers. We insert it into the large-opening end of the V-grooves around the bottom mirror and push it into the slot, where the feet of side mirror 1 are grabbed by the springs beside the V-grooves. Then we pick up side mirror 2 and insert into the perpendicular V-grooves. When both mirrors are pushed to the end of V-grooves, the spring-loaded protrusion on one side mirror is locked into the notch on the other side mirror and these spring-loaded structures ensure that the side mirrors remain in correct alignment. This assembly process can be completed within several minutes under a stereomicroscope. After assembly, we use a probe station to finely tune the position of side mirrors and use UV-curable epoxy to secure the side mirrors to the chip. As silicon reflects only about 30% of visible light, we can evaporate a 50 nm-thick layer of gold either before or after assembly without masking, to improve the optical performance of the CCRs.

III. Performance of Fabricated CCRs

In the Smart Dust project, the CCR needs to operate with an actuation voltage less than 5 V, to be compatible with solar cell power and low-voltage CMOS control signals. The modulation speed of the CCR should be in the range of several kb/s. Most importantly, the optical performance of CCR has to be good enough to transmit a signal for several hundred meters with low bit-error probability.

A. DC and AC Actuation of Fabricated CCRs

The deflection of the actuated mirror takes place under the resultant of the electrostatic torque and spring torque. A gap-closing actuator, suspended by two torsional beams, has pull-in position and pull-in voltage of [9]

$$\theta_{pull-in} = 0.4404 \frac{g}{W_m} \tag{1}$$

$$V_{pull-in} = \left(\frac{9.685 K_\theta \theta_{pull-in}^3}{\varepsilon_0 L_m} \right)^{\frac{1}{2}} \tag{2}$$

where g is the actuator gap, i.e., the thickness of buried oxide layer in the SOI wafer. Here, W_m and L_m are the width and length of the actuator plate, and K_θ is the torsional spring constant.

Fig. 4 shows experimental results of deflection angle versus applied voltage, as well as the theoretical relationship. Experiments demonstrate a DC pull-in voltage as low as 4.7 V and a pull-in angle of approximately $0.4 \cdot g/W_m$, in good agreement with theoretical predictions. Notice that the full angular travel of the actuator is g/W_m, which is several mrad for a gap distance of 2 μm and an actuator width of 300 μm. The difference between the experimental and theoretical values of the full angular travel results from the existence of the gap-closing stops.

The mechanical resonant frequency of the actuated plate is given by

$$f = \frac{1}{2\pi} \left(\frac{k_\theta}{I_m} \right)^{\frac{1}{2}} \tag{3}$$

where I_m is the moment of inertia of the actuated plate.

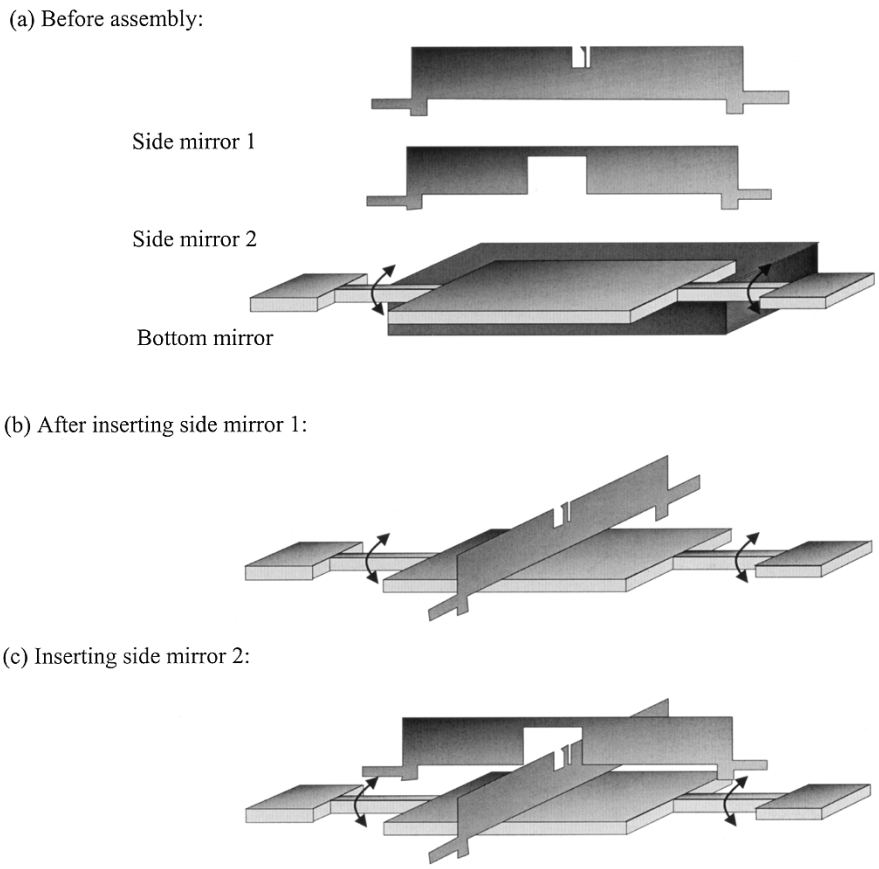

Fig. 3. Assembly sequence. Snap locks yield alignment accuracy better than 1 mrad.

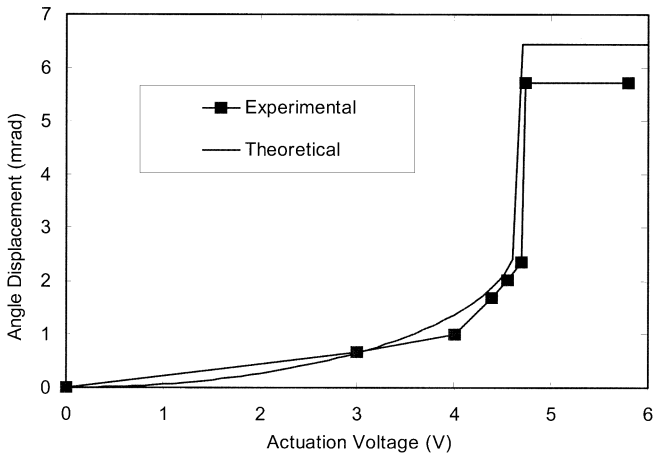

Fig. 4. Actuator angular displacement vs. applied DC actuation voltage.

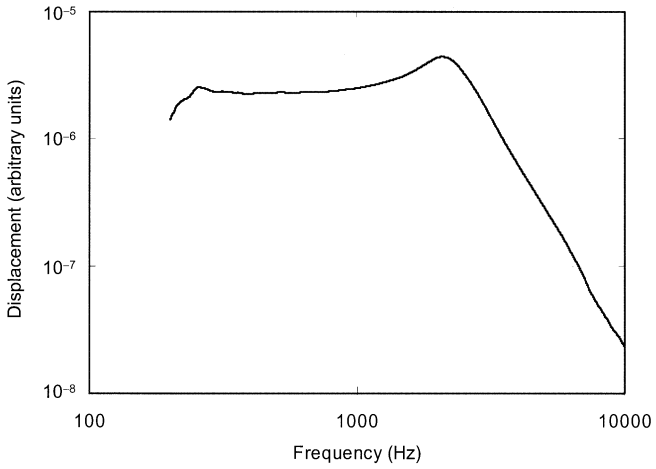

Fig. 5. Frequency response of the actuated bottom mirror plate.

Fig. 5 shows the frequency response of one device, measured using a POLYTEC laser Doppler vibrometer. A pure sinusoidal voltage source is applied to the gap-closing actuator and a lock-in amplifier senses the output signal at twice the frequency of the drive signal. Electrical resonance occurs at 2.2 kHz, corresponding to a mechanical resonant frequency of 4.4 kHz, because the actuation torque is proportional to V^2, so that the torque is applied at twice the frequency of the electrical drive signal. The electrical 3-dB cut-off frequency is around 3.5 kHz. This corresponds to a mechanical cut-off frequency of about 7.0 kHz, implying that the CCR can be digitally modulated up to about 7 kb/s. A much higher modulation speed could be achieved by fabricating the bottom mirror on a SOI wafer having a decreased device-layer thickness, with little or no impact on other performance characteristics of the CCR.

Fig. 6 shows the response of a CCR to a 250 Hz square wave. At $t = 0.5$ ms, the actuation voltage is turned off. The actuated mirror is restored to its relaxed position under the restoring

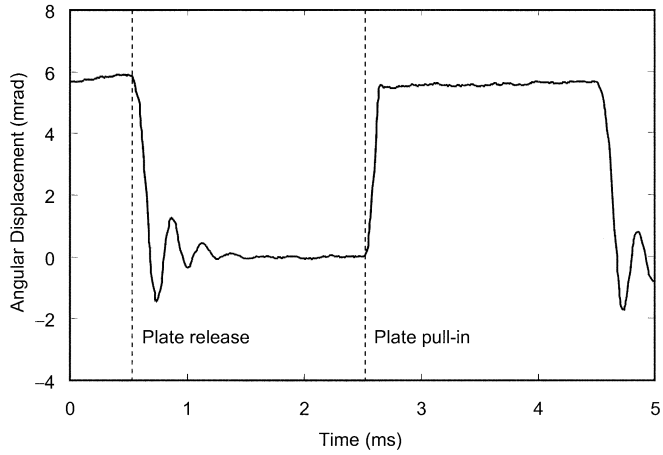

Fig. 6. Response of the actuated bottom mirror plate to a 250 Hz square wave.

torque of the torsional springs, turning on the beam reflected from the CCR. At $t = 2.5$ ms, the actuation voltage is turned on, pulling down the actuated mirror, and turning off the beam reflected from the CCR. Both release and pull-down exhibit transition times of about 55 μs. When the mirror is released, it exhibits ringing for about 1 ms before settling to the relaxed position. The 1 ms settling time implies a maximum modulation rate of about 1 kb/s. Fortunately in this process we can add an isolated substrate area under the actuated plate to obtain increased squeeze-film damping after release of the actuation voltage. We have demonstrated that this can greatly reduce the settling time, permitting the maximum modulation speed to be limited only by the resonant frequency.

A major goal of the Smart Dust project [10] is to minimize the energy per bit required for transmission. The capacitance of the CCR changes from around 1.3 pF before pull-in to 3 pF after pull-in. The actuation voltage is around 5 V. A rough estimate of the energy expended during each pull-in action is $CV^2 \approx 75$ pJ (no energy is required to release the CCR). Assuming nonreturn-to-zero encoding, energy is required only when the transmitted bit transitions from "1" to "0", so that the average energy consumption is about 19 pJ/bit. This compares quite favorably to other (RF) approaches such as Bluetooth, which has a fundamental transmission cost of 1 nJ/bit over a few 10 s of meters.

B. Optical Performance of Fabricated CCRs

A useful parameter describing the optical performance of CCR is the differential scattering cross section (DSCS). It is defined as [11]:

$$\frac{d\sigma}{d\Omega_o}(\hat{n}_i, \hat{n}_o) = \frac{I_o L^2}{I_i} \tag{4}$$

where $\hat{n}_i$ is the incident light direction, $\hat{n}_o$ is the reflected light direction, I_i is the light intensity incident on the CCR, I_o is the reflected light intensity at the observation plane and L is the distance between the CCR and the observation plane. Note that the DSCS has dimensions of m^2/sr. The DSCS depends on the mirror dimensions, mirror flatness, mirror surface quality, mirror reflectivity, and relative alignment between the mirrors. In addition, the DSCS depends on the directions of the incident and reflected beams. For a CCR with three identical square mirrors, the DSCS is largest for incident and reflected directions close to the body diagonal, i.e., $\hat{n}_i$ and $\hat{n}_o$ near $1/(\sqrt{3})(1,1,1)$.

If we illuminate an unactuated CCR with laser light, the far-field diffraction pattern corresponds to the DSCS for reflected light directions $\hat{n}_o$ close to $-\hat{n}_i$. Fig. 7(a) shows the measured far-field diffraction pattern of an unactuated CCR, with illumination along the body diagonal direction, while Fig. 7(b) shows the simulated diffraction pattern for a perfect CCR of the same size [11]. The illumination wavelength is 632.8 nm. Both measured and simulated patterns exhibit similar "star" patterns, corresponding to an effective reflecting area that is a six-sided polygon. The angular separation between nulls is 1.2 mrad in the experiment, and 1.0 mrad in the simulation, showing good agreement. The experimental results demonstrate that any angular misalignment between the mirrors must be smaller than 1 mrad, or else we would not be able to observe the diffraction pattern with null spacing on the order of 1 mrad.

The collinear DSCS (CDSCS) is defined as the value of the DSCS when the directions of illumination and observation are collinear, i.e., $\hat{n}_o = -\hat{n}_i$. The CDSCS is relevant because in CCR-based links, the receiver is usually placed along the axis of illumination. If the distance L is sufficiently large, then the receiver subtends a small solid angle Ω_o, over which the DSCS is approximately equal to the CDSCS. Under these assumptions, the received power P_o can be computed approximately using

$$P_o \approx I_i \cdot \frac{d\sigma}{d\Omega_o}(\hat{n}_i, -\hat{n}_i) \cdot \Omega_o. \tag{5}$$

For example, if a CCR consists of three identical square mirrors having side length a and reflectivity r_m, and is illuminated along the body diagonal by light at wavelength λ, the CDSCS is

$$\frac{d\sigma}{d\Omega_o}\left(\frac{1}{\sqrt{3}}(1,1,1), -\frac{1}{\sqrt{3}}(1,1,1)\right) = \frac{3a^4 r_m^3}{\lambda^2}. \tag{6}$$

In (6), we see that the CDSCS is proportional to the power captured by the CCR (a factor a^2) and the power reflected in three bounces from the mirrors (a factor r_m^3), and is inversely proportional to the solid angle into which light is diffracted from the CCR (a factor λ^2/a^2).

At a wavelength of 632.8 nm, uncoated silicon has a reflectivity of approximately 0.3, while gold has a reflectivity of 0.99. For an ideal CCR with a 250 μm bottom mirror and 450 μm

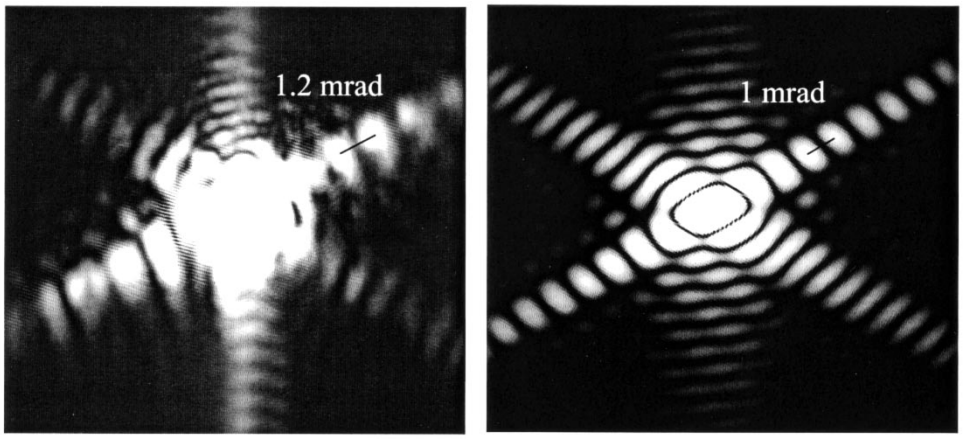

(a) (b)

Fig. 7. Far-field patterns of light reflected from CCR. (a) Experimental result for a fabricated device. (b) Theoretical result for a perfect CCR of the same size. The diffraction pattern demonstrates good alignment between the three mirrors of the CCR. The misalignment is well under half of the angle separation between different diffraction orders, i.e., less than 1 mrad.

side mirrors[1] illuminated along the body diagonal, Fraunhofer diffraction theory predicts CDSCS values of 1.2×10^{-3} m^2/sr and 4.4×10^{-2} m^2/sr for uncoated and gold-coated devices, respectively. We have experimentally measured CDSCS values of 9.3×10^{-4} m^2/sr and 2.8×10^{-2} m^2/sr, for uncoated and gold-coated devices, respectively. These measured values are close to the theoretical predictions, further confirming the near-ideal optical quality of the fabricated CCRs.

We have realized free-space optical communication over a range of 180 m. The optical setup is shown in Fig. 8(a). A continuous-wave laser (CW) beam with 632.8 nm wavelength, 0.8 mW power and 0.1 mrad divergence (half-angle) is directed toward CCR by a small mirror placed in front of the telescope. The telescope has an entrance aperture of 8 cm diameter, subtending a half-angle of 0.22 mrad at the CCR. When the CCR bottom mirror is not actuated, the beam reflected back to the telescope has a divergence (half-angle) of 0.7 mrad; when the mirror is actuated by 5.7 mrad,, this reflected beam splits apart into two beams, each directed 11.4 mrad away from the optical axis, well away from the telescope entrance aperture. As the size of the directing mirror in front of the telescope is small compared to the aperture of the telescope, the amount of light signal blocked by the directing mirror is minimal compared to the amount of signal collected by the telescope. The CCR is driven by a pseudorandom, nonreturn-to-zero bit sequence at 400 b/s. Light collected by the telescope passes through an optical bandpass filter having 632.8 nm center wavelength and 10 nm bandwidth, and is imaged onto a silicon photodiode with dimensions of 0.81 mm $\times$ 1.37 mm, which is coupled to a transimpedance amplifier. Fig. 8(b) shows the transmitted bit pattern and the detected optical signal. The modulated signal is received with high signal-to-noise ratio, although its amplitude fluctuates slowly due to air turbulence in the optical path.

[1]In devices fabricated to date, the dimensions of the side mirror are slightly larger than those of the bottom mirror because the bottom mirror is minimized to minimize layout area.

IV. Signal-to-Noise Ratio (SNR) Analysis of CCR-Based Links

In this section, we present an analysis of the SNR of free-space optical links using CCR transmitters, to identify critical design parameters and aid in design optimization. Here, we neglect the effects of atmospheric turbulence. These effects may be negligible for short-range indoor links. For outdoor links with ranges up to a few hundred meters, turbulence-induced intensity fluctuations may often be overcome simply by an increase in transmitted power, as in the example of Fig. 8(b).

Our analysis considers a system design as in Fig. 8(a). A CW laser beam with power P_i and divergence half-angle θ_i, is incident on the CCR from a range L. The intensity I_i, incident on the CCR is

$$I_i = \frac{P_i}{\pi L^2 \tan^2 \theta_i}. \tag{7}$$

The telescope has light collection area A_c. We assume that L is sufficiently large, and that A_c is sufficiently small, that the intensity of light reflected from the CCR is constant over the telescope aperture. Since the telescope subtends a solid angle $\Omega_o = A_c/L^2$ at the CCR, using (5), the telescope collects a signal power

$$P_{sig} = \frac{P_i A_c}{\pi L^4 \tan^2 \theta_i} \frac{d\sigma}{d\Omega_o}(\hat{n}_i, -\hat{n}_i) \tag{8}$$

when the CCR is not actuated (logical "1"). The telescope is assumed to collect negligible signal power when the CCR is actuated (logical "0"). Assuming the photodetector has responsivity R, when the CCR is not actuated (logical "1"), the signal photocurrent is

$$i_{sig} = \frac{P_i A_c R}{\pi L^4 \tan^2 \theta_i} \frac{d\sigma}{d\Omega_o}(\hat{n}_i, -\hat{n}_i). \tag{9}$$

Hereafter, for concreteness, we assume that the CCR consists of three identical square mirrors having side length a and reflectivity r_m, and is illuminated along the body diagonal by light at

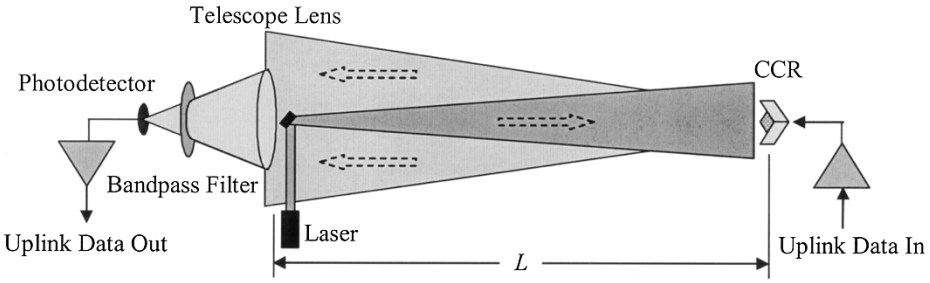

(a)

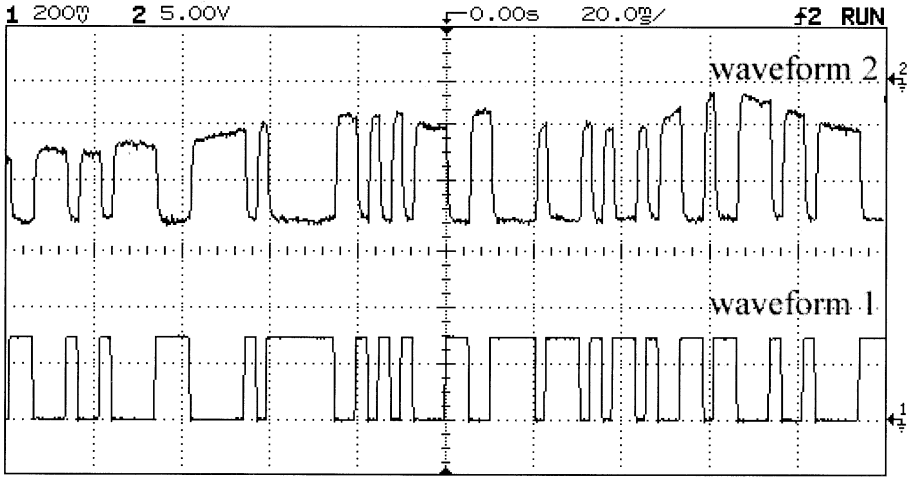

(b)

Fig. 8. (a) Optical setup for uplink free-space optical communication using a CCR as a passive transmitter. (b) Detected 400 b/s signal after free-space transmission over 180 m. Waveform 1: CCR drive signal; Waveform 2: detected photocurrent, which is proportional to the intensity reflected from CCR.

wavelength λ. In this case, the CDSCS is given by (6). Thus, the signal photocurrent when the CCR is unactuated (logical '1') is given by

$$i_{sig} = \frac{3P_i a^4 r_m^3 A_c R}{\pi \lambda^2 L^4 \tan^2 \theta_i}. \tag{10}$$

Note that the signal photocurrent is proportional to the laser power P_i. Because the beam is subject to diffractive spreading when propagating both to and from the CCR, the photocurrent depends on the transmission range as L^{-4}, instead of the L^{-2} dependence usually observed in free-space optical links. The photocurrent depends on mirror size as a^4, mirror reflectivity as r_m^3 and on wavelength as λ^{-2}, for reasons explained previously.

We now calculate the ambient light noise received by the photodetector. Suppose that the photodetector has area A_d, and that the telescope has focal length f. The area in the CCR plane "seen" by the photodetector is

$$A_f = \frac{A_d L^2}{f^2}. \tag{11}$$

Assume that the region surrounding the CCR is illuminated by ambient light having spectral density p_{bg} (this quantity represents power per unit area per unit wavelength, and has units of $\mathrm{W}/(\mathrm{m}^2 \cdot \mathrm{nm})$), and that this region reflects ambient light with reflectivity r_{bg}. Suppose that the telescope employs an optical bandpass filter having bandwidth $\Delta\lambda$. Within the filter bandwidth, the total ambient light power reflected from the region "seen" by the photodetector is

$$P_{bg} = p_{bg} R_{bg} \Delta\lambda A_f = \frac{P_{bg} r_{bg} \Delta\lambda A_d L^2}{f^2}. \tag{12}$$

Assuming that the region surrounding the CCR is a Lambertian reflector [12], the power P_{bg} results in an irradiance at the telescope of

$$I_{bg} = \frac{P_{bg}}{\pi L^2} = \frac{P_{bg} r_{bg} \Delta\lambda A_d}{\pi f^2}. \tag{13}$$

Hence, the ambient light-induced photocurrent is

$$i_{bg} = I_{bg} A_c R = \frac{P_{bg} r_{bg} \Delta\lambda A_d A_c R}{\pi f^2}. \tag{14}$$

Note that the ambient light photocurrent is independent of the transmission range L, but is proportional to the photodetector area A_d and to the telescope light-collection area A_c. In order to minimize ambient light noise, it is desirable to choose the photodetector to be only as large as required to capture the entire CCR image.

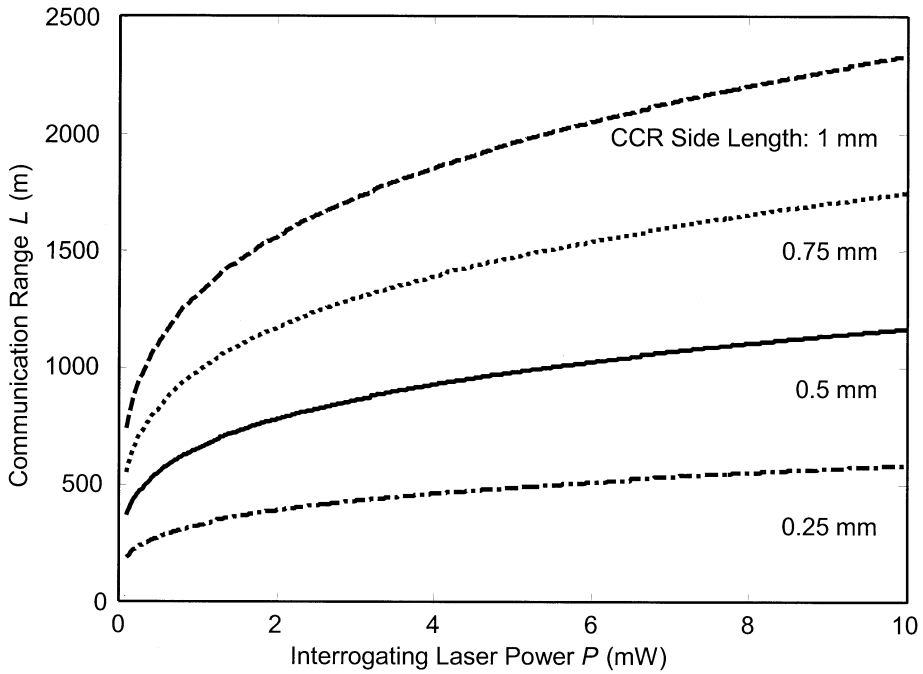

Fig. 9. Communication range L versus interrogating laser power P_i required to achieve a bit-error probability $P_b = 10_{-6}$ for different CCR side lengths (assuming that the CCR consists of three equal-sized square mirrors). We assume a bit rate of 1 kb/s and a receiver bandwidth $B = 1$kHz. All other important parameters, including interrogating beam divergence, collecting lens aperture, and photodiode dimensions, are assumed to be the same as those in the free-space communication experiment.

We assume that a preamplifier is employed to amplify the received photocurrent, and will refer all noises to the preamplifier input. The ambient light induces white shot noise, which has a (one-sided) power spectral density (PSD) given by:

$$S_{bg} = 2qi_{bg}. \tag{15}$$

Additional noises may be contributed by the preamplifier. A feedback or load resistance R_F will contribute white noise having PSD $S_R = (4k_BT)/(R_F)$, where k_B is Boltzmann's constant and T is absolute temperature. The preamplifier transistors are assumed to contribute white noise with PSD $S_{\rm amp}$. Assume that the preamplifier (or a following lowpass filter) limits the noise bandwidth to a (one-sided) bandwidth B, where B is approximately equal to the bit rate. Then the total noise variance is given by

$$\sigma^2_{\rm tot} = (S_{bg} + S_R + S_{\rm amp})B. \tag{16}$$

The peak electrical SNR is

$$\mathrm{SNR} = \frac{i^2_{\rm sig}}{\sigma^2_{\rm tot}}. \tag{17}$$

Assuming that all noise sources are Gaussian distributed, the bit-error probability is given by

$$P_b = Q\left(\frac{\sqrt{\mathrm{SNR}}}{2}\right) \tag{18}$$

where $Q(x) = 1/2$ erfc$(x/(\sqrt{2}))$. Achieving a bit-error probability of 10^{-6} requires a peak SNR of about 19.5 dB. Fig. 9 plots the relationship between the interrogating laser power P_i and the maximum transmission range L, assuming a bit-error probability $P_b = 10^{-6}$, for different values of the CCR side length a. We assume a bit rate of 1 kb/s, and assume a transimpedance receiver having bandwidth $B = 1$ kHz and feedback resistance $R_F = 20$ MΩ. All other important parameters, such as interrogating beam divergence, collecting lens aperture, and photodiode dimensions, are assumed to be the same as those in the free-space communication experiment, described in the previous section. The noise is dominated by approximately equal contributions from ambient light shot noise and thermal noise from the feedback resistor, while amplifier noise is negligible. As illustrated in the Fig. 9, the maximum transmission range L depends on the laser power as $P_i^{-1/4}$, and depends linearly on the CCR side length a. Fig. 9 demonstrates that a CCR-based link of several hundred m range is feasible.

V. Integration Into Sensor Nodes

Micromachined CCRs have been packaged with other components of Smart Dust "motes," i.e., solar cell, 1 Mb/s CMOS optical receiver, finite-state machine counter, low-power ADC, accelerometer and light-level sensor, to form a 16-mm^3 autonomous solar-powered sensor mote [5], as shown in Fig. 10(a). Each mote consists of three dies, a 0.25-μm CMOS ASIC die, a 2.6-mm^2 SOI solar cell array chip, and a MEMS four-quadrant CCR die. The mote has successfully sampled photosensor data and transmitted it over the optical link with the CCR under the illumination of one sun, or under incandescent or LED illumination of equivalent intensity.

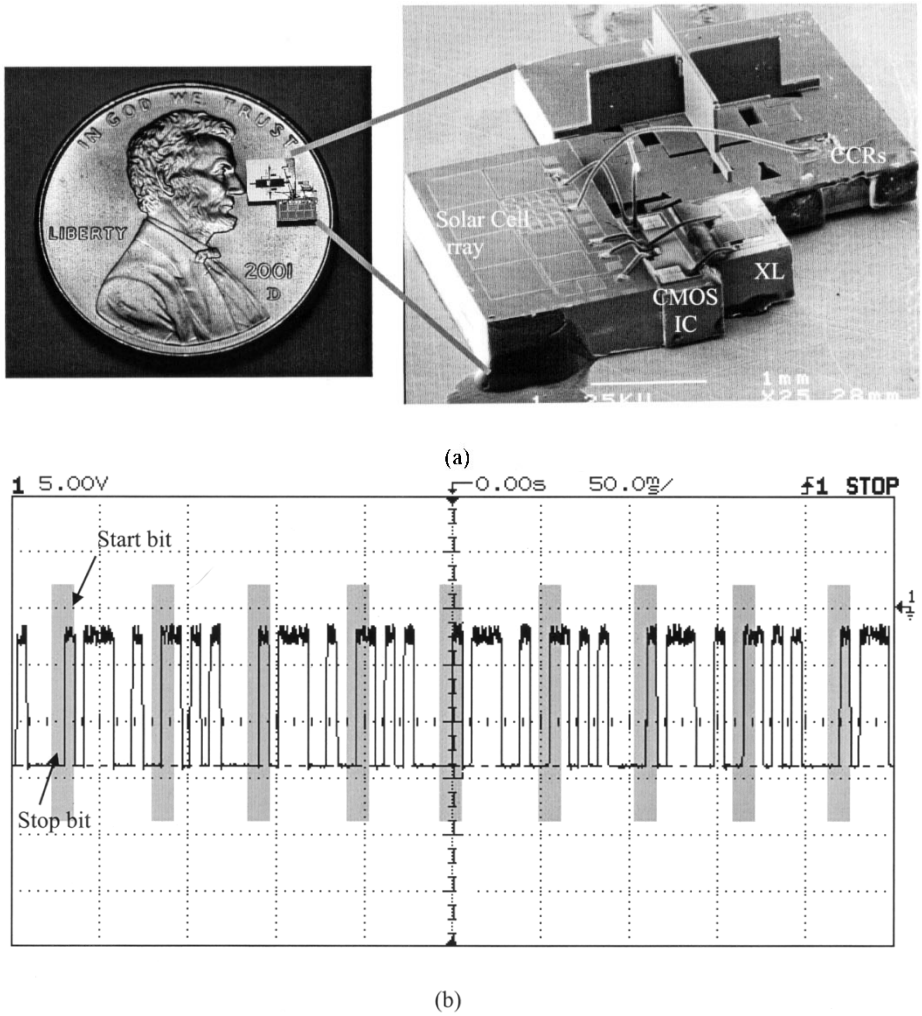

Fig. 10. (a) 16 mm^3 solar-powered sensor mote with bi-directional optical communication. Components include a multi-junction solar power array, 1 Mb/s optical receiver, CCR for optical transmitter, 8-bit ADC, digital controller, accelerometer and light-level sensor. (b) Detected data packets transmitted at 182 b/s from the mote by the modulation of CCR mirror and received using a photodiode detector. Start ("1") and stop ("0") bits from each packet are highlighted.

In the Smart Dust communication architecture, a single base station transmits commands and queries to a collection of motes via a broadcast free-space optical downlink at bit rate up to 1 Mb/s. The base station also illuminates the CCRs and uses a telescope and photodiode to receive messages transmitted via the CCR-based uplink at a bit rate approximately 180 b/s. If the base station is equipped with an imaging receiver incorporating multiple pixels, it can decode uplink messages transmitted simultaneously and without synchronization by multiple dust motes, a form of space-division multiplexing.

Fig. 10(b) shows a signal transmitted by a CCR and received by a base-station receiver. The 8-bit data packets alternately transmit data sensed by the accelerometer and light-level sensor. Data packets are separated by a stop bit "0" and a start bit "1." The asynchronous transmission data rate is approximately 182 b/s, and is determined by the clock frequency of the internal oscillator in the ASIC chip.

VI. Conclusion

The modulated CCRs presented here have performance substantially better than any previously presented, largely due to the accurate alignment made possible by spring-loaded assembly of SOI side mirrors. The actuation voltage, less than 5 V, is compatible with solar cell power and CMOS control switches. The energy consumption, which averages 19 pJ per bit, is consistent with the power requirements of a millimeter-scale autonomous sensor node. The optical performance of the CCRs is sufficient to allow interrogation from hand-held equipment at ranges of hundreds of meters.

Acknowledgment

The authors are grateful for the help of G. Wang, J. Wang, V. Hsu, V. Milanovic, C. Keller, M. Last, B. Warneke, M. Scott, and B. Leibowitz.

References

[1] A. Acampora, "Last mile by laser," *Sci. Amer. (International Edition)*, vol. 286, no. 7, pp. 32–37, 2002.
[2] W. R. Leeb, "Laser space communications: systems, technologies, and applications," *Rev. Laser Eng.*, vol. 28, no. 12, pp. 804–808, 2000.
[3] C. DeCusatis, "Optical data communication: fundamentals and future directions," *Opt. Eng.*, vol. 37, no. 12, pp. 3082–3099, 1998.
[4] "Rand Report,", Santa Monica, CA, 1993.

[5] B. A. Warneke, M. D. Scott, B. S. Leibowitz, L. Zhou, C. L. Bellew, J. A. Chediak, J. M. Kahn, B. E. Boser, and K. S. J. Pister, "An autonomous 16 mm^3 solar-powered node for distributed wireless sensor networks," in *Proc. Sensor 2002*, Orlando, FL, June, 12–14 2002.
[6] K. S. J. Pister, M. W. Judy, S. R. Burgett, and R. S. Fearing, "Microfabricated hinges," *Sens. Actuators: Phys. A*, vol. A33, no. 3, pp. 249–256, 1992.
[7] P. B. Chu, N. R. Lo, E. C. Berg, and K. S. J. Pister, "Optical communication using micro corner cube reflectors," in *Proc. IEEE Micro Electro Mechanical Systems Workshop*, Nagoya, Japan, 1997, pp. 350–355.
[8] L. Zhou, K. S. J. Pister, and J. M. Kahn, "Assembled corner-cube retroreflector quadruplet," in *Proc. 2002 IEEE MEMS Conf.*, Las Vegas, NV, Jan., 20–24 2002, pp. 556–559.
[9] O. Degani and Y. Nemirovsky, "Design considerations of rectangular electrostatic torsion actuators based on new analytical pull-in expressions," *J. Microelectromech. Syst.*, vol. 11, no. 1, pp. 20–26, 2002.
[10] L. Doherty, B. A. Warneke, B. E. Boser, and K. S. J. Pister, "Energy and performance considerations for Smart Dust," *Int. J. Parallel Distrib. Syst.*, vol. 4, no. 3, pp. 121–133, 2001.
[11] X. Zhu, V. S. Hsu, and J. M. Kahn, "Optical modeling of MEMS corner-cube retroreflectors with misalignment and nonflatness," *IEEE J. Select. Topics Quantum Electron.*, vol. 48, no. 1, pp. 26–32, Jan./Feb. 2002.
[12] M. Born and E. Wolf, *Principles of Optics*, 6th ed. New York: Pergamon, 1980.

Lixia Zhou received the B.S. degree in applied physics and the B.E. degree in computer science and technology from Tsinghua University in 1996. She received the M.S. degree in electrical engineering and computer science from the University of California at Berkeley in 2002. She is currently pursuing the Ph.D. degree in electrical engineering and computer science at the University of California at Berkeley.

Her current research interests include MEMS self-assembly, fabrication process, and MEMS micromirror design.

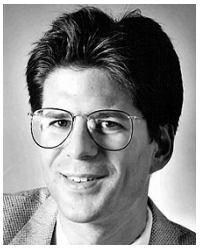

Joseph M. Kahn (M'90–SM'98–F'00) received the A.B., M.A., and Ph.D. degrees in physics from the University of California at Berkeley in 1981, 1983, and 1986, respectively.

He is currently a Professor in the Department of Electrical Engineering at Stanford University, Stanford, CA. Previously, he was a Professor in the Department of Electrical Engineering and Computer Sciences at University of California at Berkeley. In 2000, he co-founded StrataLight Communications, Inc., where he is currently Chief Scientist. From 1987 to 1990, he was a Member of Technical Staff in the Lightwave Communications Research Department of AT&T Bell Laboratories, where he performed research on multigigabit per second coherent optical fiber transmission systems, setting world records for receiver sensitivity. His current research interests include optical fiber communication, free-space optical communication, and wireless communication for sensor networks based on microelectromechanical systems.

Prof. Kahn received the National Science Foundation Presidential Young Investigator Award in 1991. He is a Member of the IEEE Communications Society and the IEEE Lasers and Electro-Optics Society. From 1993 to 2000, he served as a Technical Editor of *IEEE Personal Communications Magazine*.

Kristofer S. J. Pister (M'03) received the B.A. degree in applied physics from the University of California at San Diego in 1982 and the M.S. and Ph.D. in electrical engineering from the University of California at Berkeley in 1989 and 1992, respectively.

From 1992 to 1997, he was an Assistant Professor of Electrical Engineering at the University of California at Los Angeles. He is now a Professor of Electrical Engineering and Computer Sciences at the University of California at Berkeley. He has been a member of the DARPA ISAT and JASON groups, and the Defense Science Study Group.